Draft version April 8, 2026
Typeset using LaTeX **twocolumn** style in AASTeX7.0.1

arXiv:2601.15452v3 [astro-ph.HE] 6 Apr 2026

The long quest for vacuum birefringence in magnetars: 1E 1547.0−5408 and the elusive smoking gun

Roberto Taverna [1], Roberto Turolla [1,2], Lorenzo Marra [3], Ruth M.E. Kelly [2], Alice Borghese [4], Gian Luca Israel [5], Sandro Mereghetti [6], Andrea Possenti [7], Silvia Zane [2] and Michela Rigoselli [8,6]

[1] *Department of Physics and Astronomy, University of Padova, via Marzolo 8, I-35131 Padova, Italy*
[2] *Mullard Space Science Laboratory, University College London, Holmbury St Mary, Dorking, Surrey RH5 6NT, UK*
[3] *INAF - Istituto di Astrofisica e Planetologia Spaziali, Via del Fosso del Cavaliere 100, I-00133, Roma*
[4] *European Space Agency (ESA), European Space Astronomy Centre (ESAC), Camino Bajo del Castillo s/n, 28692 Villanueva de la Cañada, Madrid, Spain*
[5] *INAF - Osservatorio Astronomico di Roma, via Frascati 33, I-00078 Monteporzio Catone, Italy*
[6] *INAF - Istituto di Astrofisica Spaziale e Fisica Cosmica di Milano, via Corti 12, I-20133 Milano, Italy*
[7] *INAF - Osservatorio Astronomico di Cagliari, via della Scienza 5, I-00947 Selargius, Italy*
[8] *INAF - Osservatorio Astronomico di Brera, via Brera 28, I-20121 Milano, Italy*

ABSTRACT

Magnetars are now known to be among the most strongly polarized celestial sources in X-rays. Here we report on the 500 ks observation of the magnetar 1E 1547.0−5408 performed by the Imaging X-ray Polarimetry Explorer (*IXPE*) in March 2025. The *IXPE* spectrum is well reproduced by a single thermal component with blackbody temperature $kT_{\rm BB} \sim 0.67$ keV and emission radius $R_{\rm BB} \sim 1.2$ km. The source exhibits a high linear polarization degree in the 2–6 keV band (PD $= 47.7 \pm 2.9\%$) with polarization angle PA $= 75^\circ.8 \pm 1^\circ.8$, measured West of celestial North. While PA does not appear to vary with energy, there is some evidence (at the 1σ confidence level) of a minimum in PD between 3 and 4 keV, compatible with what is expected by partial mode conversion at the vacuum resonance in a magnetized atmosphere. Phase-resolved spectral and polarimetric analyses reveal that X-ray thermal radiation likely originates from a single, fairly small hot spot with a non-uniform temperature distribution. Fitting the phase-dependent PA measured by *IXPE* with a rotating vector model (RVM) constrains the source geometry and indicates that both the dipole axis and line-of-sight are misaligned with respect to the spin axis. Under these conditions, the high polarization of the source cannot be regarded as compelling evidence for the presence of vacuum birefringence in the star magnetosphere. Nevertheless, the fact that the RVM successfully reproduces the modulation of the X-ray polarization angle and the behavior of PD with the energy hint once more to the presence of QED effects in magnetars.

Keywords: Magnetars (992) — Neutron Stars (1108) — Polarimetry (1278) —Single x-ray stars (1461)

1. INTRODUCTION

Soft gamma repeaters (SGRs) and anomalous X-ray pulsars (AXPs) form a distinct class of Galactic X-ray pulsars characterized by long rotational periods, $P \approx 1$–12 s, and large spin-down rates, $\dot{P} \approx 10^{-15}$–10^{-10} s s^{-1}. These sources produce recurrent, sub-second bursts of hard X-ray/soft-γ radiation and exhibit persistent X-ray luminosities of $L_{\rm X} \approx 10^{30}$–$10^{35}$ erg s^{-1}, typically exceeding their rotational energy losses. Their timing properties imply surface dipole magnetic fields of $B \approx 10^{13}$–10^{15} G, and the absence of detectable companions identifies them as magnetars: neutron stars powered primarily by the decay and dissipation of ultra-strong magnetic fields (R. C. Duncan & C. Thompson 1992; C. Thompson & R. C. Duncan 1993, see also R. Turolla et al. 2015; V. M. Kaspi & A. M. Beloborodov 2017 for reviews).

Below ~ 10 keV, magnetar spectra are commonly represented by two-component models, either two blackbodies or a blackbody plus a power law. The thermal components arise from localized hot spots on the neutron star surface, whereas the non-thermal component is produced via resonant Compton scattering (RCS) of surface photons by magnetospheric charges in a twisted magnetic field (C. Thompson et al. 2002; R. Fernández &

C. Thompson 2007; L. Nobili et al. 2008). Many magnetars also emit a hard X-ray tail extending up to $\sim$ 100–200 keV, often with strong pulsations.

In such extreme magnetic environments, the propagation of electromagnetic radiation is profoundly modified, as first discussed in the pioneering work of Y. N. Gnedin et al. (1978a,b, see also J. S. Heyl & L. Hernquist 1997 and A. K. Harding & D. Lai 2006 for a comprehensive review). The combined plasma–vacuum dielectric tensor becomes highly anisotropic, and the ordinary (O) and extraordinary (X) polarization eigenmodes acquire markedly different opacities. Radiative-transfer calculations predict correspondingly large linear polarization fractions, up to $\sim 80\%$ and $\sim 20\%$, from thermal emission emerging from strongly magnetized atmospheres or condensed surfaces, respectively (e.g., R. Fernández & S. W. Davis 2011; R. Taverna et al. 2014, 2020). Until recently, these predictions remained untested, owing to the lack of sensitivity in X-ray polarimeters.

The launch of the Imaging X-ray Polarimetry Explorer (*IXPE*) in December 2021 (M. C. Weisskopf et al. 2022) enabled the first high-quality spectro-polarimetric measurements in the 2–8 keV band. During its four years of operations, *IXPE* observed about one hundred X-ray sources, including five persistent magnetars, 4U 0142+61 (R. Taverna et al. 2022), 1RXS J170849.0−400910 (hereafter 1RXS J1708; S. Zane et al. 2023), SGR 1806−20 (R. Turolla et al. 2023), 1E 2259+586 (J. Heyl et al. 2024) and 1E 1841−045 (M. Rigoselli et al. 2025; R. E. Stewart et al. 2025a). With the exception of SGR 1806−20, statistically significant polarization (energy- and phase-integrated) was detected, ranging from $\approx 6\%$ to $\approx 35\%$. The degree of polarization is strongly dependent on the energy: it is moderate ($\approx$ 10–20%) at 2–3 keV and then increases to $\approx$ 60–80% at 6–8 keV in 1E 1841−045 and 1RXS J1708, or to $\approx 35\%$ in 4U 0142+61. The polarization angle remains nearly constant with the energy in the former two sources, implying that the same polarization mode dominates through the *IXPE* band. In contrast, 4U 0142+61 exhibits a drop in the polarization degree to zero near 4 keV accompanied by $\sim 90^\circ$ rotation of the polarization angle, signaling a transition in the prevailing polarization mode (see R. Taverna & R. Turolla 2024, for an extensive discussion and D. Lai 2023 for an alternative interpretation).

In this paper, we report on the spectral and polarization analysis of the *IXPE* observation of the magnetar 1E 1547.0−5408, targeted in the GO2 observing run (P.I. George Younes). We provide a comparative assessment of our findings against those recently presented in a preprint by R. E. Stewart et al. (2025b) and highlight similarities and differences between their (preliminary) analysis and the present one. Observations and data processing are detailed in Section 2. The results of our spectral, timing, and polarimetric analyzes are presented in Section 3 and discussed in Section 4. Conclusions follow in Section 5.

2. OBSERVATIONS AND DATA ANALYSIS

The *IXPE* observation of 1E 1547.0−5408 started on 2025 March 26 03:01:52 UTC and ended on 2025 April 5 00:26:53 UTC, for a total on-source exposure time of $\approx$ 500 ks. After retrieving the level 1 and level 2 data files from the HEASARC *IXPE* public archive[1], we referred the event arrival times to the Solar System barycenter using the ftool `barycorr` with JPL planetary ephemerids DE430 (RA = $15^{\rm h}\,50^{\rm m}\,54.12386^{\rm s}$, DEC = $-54^\circ\,18'\,24.1131''$, taken from the ATNF Pulsar Catalogue[2], R. N. Manchester et al. 2005), and performed proper background rejection, according to the procedure discussed in A. Di Marco et al. (2023); furthermore, some time intervals containing the most prominent background spikes, for a total of $\lesssim 100$ s, were removed from the data set. We then extracted from the resulting photon lists the source counts from a circle of radius $r^{\rm src}$, centered on the position of the source and subtracted the background counts taken from a concentric annular region, with inner and outer radii $r^{\rm bkg}_{\rm inn}$ and $r^{\rm bkg}_{\rm out}$, respectively. Following the procedure outlined in E. Piconcelli et al. (2004), we find that the best signal-to-noise ratio is obtained for $r^{\rm src} = 60''$, $r^{\rm bkg}_{\rm inn} = 120''$ and $r^{\rm bkg}_{\rm out} = 240''$; this produced about 25,600 source counts summed over the three *IXPE* detector units (DUs). By taking $r^{\rm src} \lesssim 50''$ an increasing fraction of the source photons is lost, up to $\sim 20\%$ when $r^{\rm src}$ shrinks to $\sim 30''$.

The source counts are completely dominated by the background above $\approx$ 6 keV, preventing a meaningful spectro-polarimetric analysis at higher energies (see §3.2). We therefore opted to restrict our investigation to the 2–6 keV energy band and to use the weighted analysis procedure. To this end, we processed the level 2 files using the latest version of the *IXPE* response functions (20250225), available online in the HEASARC calibration database[3].

3. RESULTS

3.1. *Timing analysis*

We processed the level 2 photon lists using version 8.1 of the HENDRICS package (M. Bachetti 2018, see

[1] https://heasarc.gsfc.nasa.gov/docs/ixpe/archive
[2] https://www.atnf.csiro.au/research/pulsar/psrcat
[3] https://heasarc.gsfc.nasa.gov/docs/ixpe/caldb

also M. Bachetti et al. 2015 for a complete description of the STINGRAY software), to compute the timing solution for 1E 1547.0−5408. The most prominent peak in the frequency spectrum appears in the 0.45–0.50 Hz interval, within which we then performed a Z_n^2 search. Sinusoidal pulsations were detected at a frequency $\nu_0 = 0.47785498(2)$ Hz, with a frequency derivative $\dot{\nu}_0 = -4.7(6) \times 10^{-12}$ Hz/s. The times-of-arrival (TOAs) of the events were then calculated using the `HENphaseogram` tool, dividing the observation into 75 time intervals. Finally, by fitting the TOAs with a linear spin-down relation $\nu = \nu_0 + \dot{\nu}_0 t$ with the PINT software (v1.1.4, J. Luo et al. 2021), we obtained the best-fitting spin frequency and frequency derivative as $\nu = 0.477855133 \pm 2.1 \times 10^{-8}$ Hz and $\dot{\nu} = -(4.68 \pm 0.19) \times 10^{-12}$ Hz/s (χ^2/dof = 40.832/76), respectively, at epoch 60765.0724 MJD; the corresponding values of the period and period derivative are $P = 2.092684438 \pm 9.4 \times 10^{-8}$ s and $\dot{P} = (2.05 \pm 0.08) \times 10^{-11}$ s/s [4] (for a spin-down dipole magnetic field strength $B_{\rm sd} \approx 2 \times 10^{14}$ G at the magnetic equator). This timing solution was then used to phase-fold the photon lists with the `xpphase` tool within the IXPEOBSSIM package (L. Baldini et al. 2022, see Section 3.5).

3.2. *Phase-averaged spectral analysis*

We processed data from the three *IXPE* DUs within XSPEC (K. A. Arnaud 1996), generating the Ancillary Response Files (ARFs) and Modulation Response Files (MRFs) with the IXPECALCARF tool (C.-T. Chen & IXPE Science Operation Center 2025). Data were grouped to ensure a signal-to-noise ratio $\gtrsim 3$ in each bin in the 2–6 keV energy band. A normalization factor was included in all the models to account for the different cross-calibration of the three DUs (assuming unity for DU1). Interstellar absorption was modeled using `tbabs`, with abundances taken from J. Wilms et al. (2000) and photoionization cross-sections from D. A. Verner et al. (1996). We adopted the column density $N_{\rm H} = 4.6 \times 10^{22}$ cm^{-2} quoted in the systematic study by F. Coti Zelati et al. (2020), based on *XMM-Newton*, *Chandra*, and *Swift-XRT* data collected between 2009 and 2017 (see F. Coti Zelati et al. 2018), since the limited coverage of *IXPE* at low energies does not allow a precise determination of $N_{\rm H}$. We first attempted a fit using a single absorbed blackbody (BB) component (`tbabs`×`bbodyrad`). The model shows a good agreement with the data (see Figure 1 and Table 1), with χ^2/dof = 263.95/248. The resulting blackbody temperature, ≈ 0.67 keV, is fully consistent with the values reported from observations taken shortly after the 2009 outburst of 1E 1547.0−5408 (see F. Bernardini et al. 2011). However, the corresponding emission radius, ≈ 1.2 km for a distance of 4.5 kpc (A. Tiengo et al. 2010), is somewhat smaller and more in line with the most recent estimates (F. Coti Zelati et al. 2020; M. E. Lower et al. 2023). This discrepancy is most likely due to the larger size of the emitting region during an outburst phase, which then shrinks as the source returns in quiescence (see e.g. D. De Grandis et al. 2022).

For completeness, and given that previous studies of the source at soft X-ray energies showed the presence of a second spectral component (F. Bernardini et al. 2011; F. Coti Zelati et al. 2020), we also considered adding to the model either a blackbody or a power-law (PL). Keeping $N_{\rm H}$ fixed at the above value, the fit with two blackbodies, `tbabs`×`(bbodyrad+bbodyrad)`, is also good, with χ^2/dof = 255.50/242. The spectral parameters of the softer component are well constrained and similar to those obtained previously ($kT_1 = 0.65$ keV, $R_{\rm BB_1} = 1.3$ km), while those of the hotter one are totally unconstrained. Similar results were obtained with a blackbody plus power-law model, `tbabs`×`(bbodyrad+powerlaw)`, fixing $N_{\rm H}$ to the value obtained by F. Coti Zelati et al. (2018) using a BB+2PL decomposition (4.9×10^{22} cm^{-2}). The fit is also statistically satisfactory (χ^2/dof = 253.94/242), with blackbody temperature (0.64 keV) and radius (1.4 km) compatible with those obtained before, but the non-thermal component remains completely unconstrained (see again Table 1 and Figure 1 for details).

We finally note that previous broad-band investigations of 1E 1547.0−5408 required the presence of an additional power-law component at hard X-ray energies, dominating the spectrum above ≈ 10 keV (F. Bernardini et al. 2011; F. Coti Zelati et al. 2020; M. E. Lower et al. 2023). We do not include this component in our fits, as its contribution in the *IXPE* energy range is negligible. For all these reasons, we adopted the single-BB model in the remainder of our spectro-polarimetric analysis. Although our conclusions about the spectral model agree with those of R. E. Stewart et al. (2025b), the values of $kT_{\rm BB}$ and $R_{\rm BB}$ are not compatible within 3σ, possibly due to the different values assumed for $N_{\rm H}$.

3.3. *Phase-resolved spectral analysis*

Using the IXPEOBSSIM `xpphase` and `xpselect` tools, the data were folded into seven equally-spaced phase bins, based on the timing solution presented in §3.1. We then extracted the source and background spectra in each phase bin, and, according to the results of the

[4] Here and in the following, errors are quoted at 1σ confidence level, unless explicitly stated otherwise.

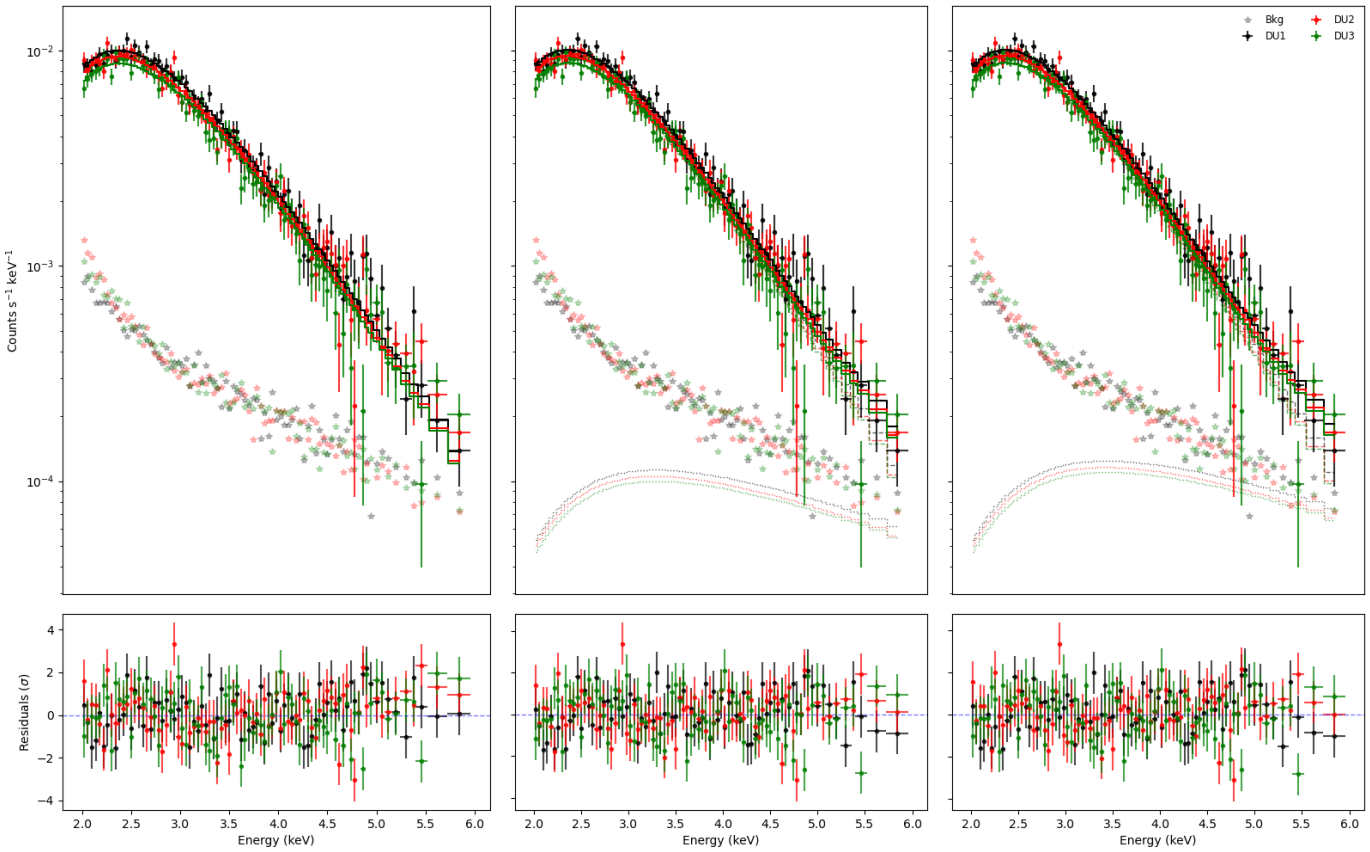

Figure 1. *IXPE* source (dots with error bars) and background (stars) spectra (top panel) of 1E 1547.0−5408 collected by DU1 (black), DU2 (red) and DU3 (green), and fitting residuals in units of the standard deviation (bottom panels) for the `tbabs`×`bbodyrad` model with $N_{\rm H}$ frozen at $4.6 \times 10^{22}\,{\rm cm}^{-2}$ (left), `tbabs`×`(bbodyrad+bbodyrad)` model with $N_{\rm H}$ frozen at $4.6 \times 10^{22}\,{\rm cm}^{-2}$ (center) and `tbabs`×`(bbodyrad+powerlaw)` model with $N_{\rm H}$ frozen at $4.9 \times 10^{22}\,{\rm cm}^{-2}$ (right). The best fitting models (solid histograms) and the individual components (dotted histograms) are also shown in each plot. Fit results are summarized in Table 1.

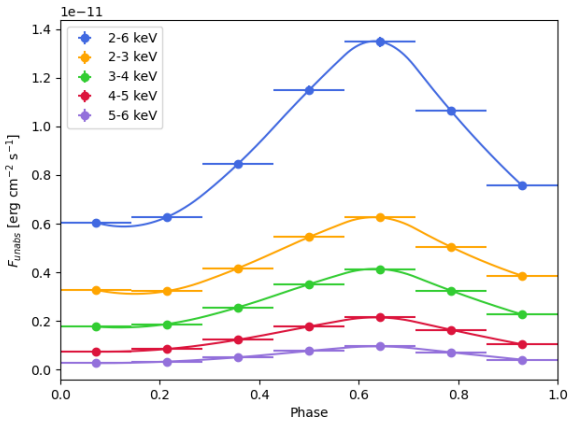

Figure 2. *IXPE* pulse-profile of 1E 1547.0−5408 in the 2–6, 2–3, 3–4, 4–5 and 5–6 keV energy bands; the solid lines are splines connecting the data.

phase-averaged analysis discussed in §3.2, we fit the data using a single-component model (`tbabs`×`bbodyrad`), with the column density $N_{\rm H}$ frozen to the value reported in Table 1[5].

Table 2 reports the best-fitting parameters for each phase bin, together with the corresponding unabsorbed and observed fluxes. The χ^2/dof values indicate that the model provides an acceptable fit at a confidence level greater than 99% in all phase bins. The pulse-profile in the 2–6 keV energy range is shown in Figure 2, along with those in the 2–3, 3–4, 4–5 and 5–6 keV energy bins. The average values of the unabsorbed and observed fluxes, $(9.14 \pm 0.07) \times 10^{-12}\,{\rm erg\,cm^{-2}\,s^{-1}}$ and $(5.70 \pm 0.04) \times 10^{-12}\,{\rm erg\,cm^{-2}\,s^{-1}}$, respectively, are consistent with the corresponding phase-averaged values (see Table 1) at 2σ confidence level. The mea-

[5] We verified that, similarly to what was found in the phase-averaged spectral analysis, a second spectral component is not statistically required.

Table 1. Phase-averaged spectral analysis of the *IXPE* data.

	`tbabs×bbodyrad`	`tbabs×(bbodyrad+bbodyrad)`	`tbabs×(bbodyrad+powerlaw)`
$N_{\rm H}$ ($10^{22}\,{\rm cm}^{-2}$)	4.6 [(a)]	4.6 [(a)]	4.9 [(a)]
kT_1 (keV)	$0.674^{+0.006}_{-0.005}$	$0.653^{+0.009}_{-0.009}$	$0.638^{+0.011}_{-0.018}$
$R^{\rm (b)}_{\rm BB_1}$ (km)	$1.20^{+0.02}_{-0.02}$	$1.27^{+0.04}_{-0.03}$	$1.36^{+0.06}_{-0.05}$
kT_2 (keV)	—	< 200	—
$R^{\rm (b)}_{\rm BB_2}$ (km)	—	$1.91^{+182.86}_{-0.20} \times 10^{-3}$	—
$\Gamma_{\rm PL}$	—	—	$-1.14^{+2.81}_{-1.10}$
$\rm norm^{(c)}_{PL}$	—	—	$3.46^{+571.08}_{-3.21} \times 10^{-6}$
$F^{2-6\ \rm (d)}_{\rm unabs}$	$9.29^{+0.07}_{-0.07}$	$9.37^{+0.07}_{-0.07}$	$9.69^{+0.07}_{-0.07}$
$F^{2-6\ \rm (e)}_{\rm obs}$	$5.81^{+0.04}_{-0.04}$	$5.87^{+0.04}_{-0.04}$	$5.87^{+0.04}_{-0.04}$
$\rm const_{DU_1}$	1.00 [(a)]	1.00 [(a)]	1.00 [(a)]
$\rm const_{DU_2}$	$1.02^{+0.02}_{-0.02}$	$1.03^{+0.02}_{-0.02}$	$1.02^{+0.02}_{-0.02}$
$\rm const_{DU_3}$	$0.95^{+0.02}_{-0.02}$	$0.95^{+0.02}_{-0.02}$	$0.95^{+0.02}_{-0.02}$
χ^2/dof	263.95/244	255.50/242	253.94/242

Note—
(a) – Frozen parameters.
(b) – Emission radius extracted from the `bbodyrad` parameter norm assuming a distance of 4.5 kpc (A. Tiengo et al. 2010).
(c) – Normalization of the `powerlaw` component in photons $\rm keV^{-1}\,cm^{-2}\,s^{-1}$ at 1 keV.
(d) – Total unabsorbed 2–6 keV flux in units of $10^{-12}\,\rm erg\,cm^{-2}\,s^{-1}$.
(e) – Total observed 2–6 keV flux in units of $10^{-12}\,\rm erg\,cm^{-2}\,s^{-1}$.

Table 2. Phase-resolved spectral fit of the *IXPE* data in the 2–6 keV band.

Spectral model: `tbabs×bbodyrad`[(a)]

phase bin	kT (keV)	$R_{\rm BB}$ (km)[(b)]	$F^{\rm (c)}_{\rm unabs}$	$F^{\rm (d)}_{\rm obs}$	χ^2/dof
0.00–0.14	$0.610^{+0.018}_{-0.017}$	$1.24^{+0.24}_{-0.23}$	$6.05^{+0.15}_{-0.15}$	$3.63^{+0.09}_{-0.09}$	127.00/131
0.14–0.29	$0.641^{+0.018}_{-0.017}$	$1.11^{+0.21}_{-0.20}$	$6.27^{+0.15}_{-0.15}$	$3.84^{+0.09}_{-0.09}$	103.07/128
0.29–0.43	$0.667^{+0.017}_{-0.017}$	$1.17^{+0.21}_{-0.19}$	$8.46^{+0.17}_{-0.17}$	$5.26^{+0.11}_{-0.11}$	128.68/149
0.43–0.57	$0.691^{+0.014}_{-0.014}$	$1.25^{+0.20}_{-0.19}$	$11.49^{+0.20}_{-0.20}$	$7.25^{+0.12}_{-0.12}$	159.02/164
0.57–0.71	$0.704^{+0.014}_{-0.013}$	$1.29^{+0.19}_{-0.18}$	$13.49^{+0.22}_{-0.22}$	$8.57^{+0.14}_{-0.14}$	164.24/178
0.71–0.86	$0.690^{+0.015}_{-0.015}$	$1.21^{+0.19}_{-0.18}$	$10.63^{+0.19}_{-0.19}$	$6.71^{+0.12}_{-0.12}$	168.32/161
0.86–1.00	$0.646^{+0.017}_{-0.017}$	$1.20^{+0.22}_{-0.20}$	$7.56^{+0.16}_{-0.16}$	$4.65^{+0.10}_{-0.10}$	148.12/137

Note—
(a) – $N_{\rm H}$ is fixed at $4.6 \times 10^{22}\,\rm cm^{-2}$ (see F. Coti Zelati et al. 2020) and the cross-calibration constants of the three *IXPE* DUs are frozen to the values reported in Table 1.
(b) – Emission radius extracted from the `bbodyrad` parameter norm assuming a distance of 4.5 kpc (A. Tiengo et al. 2010).
(c) – Total unabsorbed flux in units of $10^{-12}\,\rm erg\,cm^{-2}\,s^{-1}$.
(d) – Total observed flux in units of $10^{-12}\,\rm erg\,cm^{-2}\,s^{-1}$.

sured pulsed fraction (PF, see Table 3) increases monotonically with energy from $31.9 \pm 1.3\%$ at 2–3 keV to

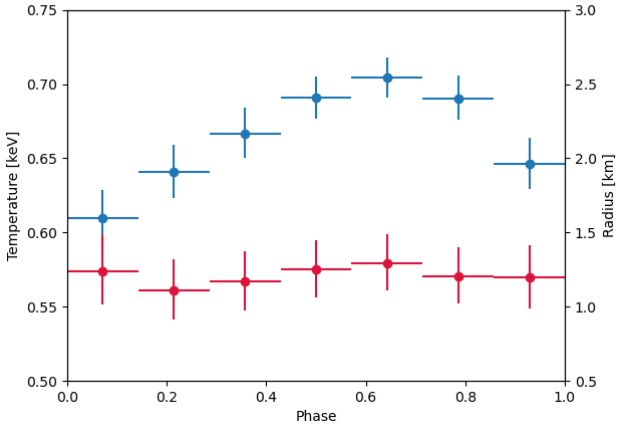

Figure 3. Phase variation of the blackbody temperature (cyan) and radius (red) for the best-fitting model reported in Table 2.

$56.5 \pm 1.0\%$ at 5–6 keV (the constant-PF hypothesis is rejected at more than 10σ). The averaged pulsed fraction in the 2–6 keV is $38.1 \pm 1.3\,\%$.

Figure 3 shows the phase dependence of the temperature and emission radius for the best-fitting spectral model. While $R_{\rm BB}$ is consistent with a constant value (1.22 ± 0.07 km) at the 1σ confidence level, in agreement with the emission radius inferred from the phase-averaged spectrum (see Table 1), the blackbody temperature shows a clear oscillation in phase with the pulse profile (see Figure 2).

3.4. *Phase-averaged polarimetric analysis*

We processed the source photon lists using the same procedure described in §3.2 and §3.3 to extract the Q and U Stokes parameters as functions of photon energy and rotational phase. We followed the method discussed in T. E. Strohmayer (2017), simultaneously fitting the I, Q, and U spectra in different energy intervals within XSPEC, with the appropriate response functions; the Q and U data were grouped in such a way to ensure at least 5 counts per energy bin. We convolved a constant polarization model (`polconst`) to the `tbabs`×`bbodyrad` model (see §3.2) and froze the spectral parameters to the values obtained in the phase-averaged spectral fit (see Table 1). We note that this method is essentially independent of the specific spectral model adopted, provided that the energy intervals in which the polarization properties are extracted are sufficiently narrow. We checked a posteriori that the PD and PA values derived using the alternative spectral models reported in Table 1 differ only marginally from those obtained using the single-BB model, with deviations well within the 1σ confidence intervals.

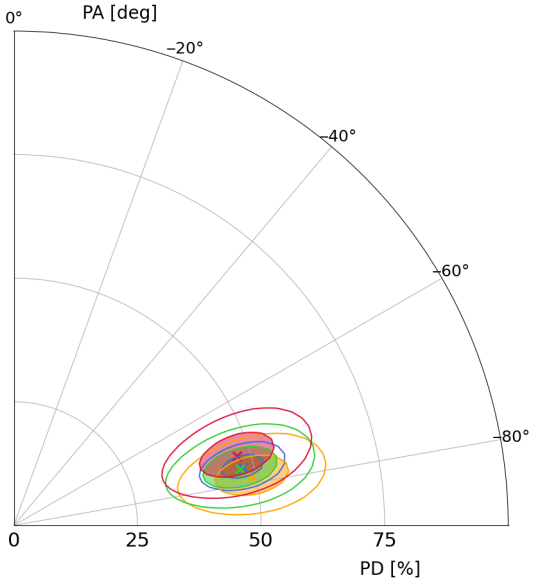

Figure 4. 1E 1547.0−5408 phase- and energy-integrated (2–6 keV) most-probable values for PD and PA (crosses) measured by the three *IXPE* DUs (DU1 yellow, DU2 green and DU3 red); the combined result is also shown in blue. Constant PD and constant PA loci are marked by concentric circles and radial lines, respectively, with PA = 0° corresponding to the celestial North, and PA decreasing Westward. The shaded and empty contours represents the 68% and 99% confidence regions, respectively, obtained using the `steppar` command in XSPEC.

The results for the phase-averaged degree and angle of polarization, integrated in the entire range 2–6 keV are shown in Figure 4 for each of the three DUs, together with the value obtained by combining the data from all DUs. The polarization degree for the combined DUs, $\mathrm{PD} = \sqrt{(Q/I)^2 + (U/I)^2}$, is $47.7 \pm 2.9\%$ and is significant at the level $\approx 16\sigma$. The associated polarization angle, $\mathrm{PA} = \arctan(U/Q)/2$ is $75°.8 \pm 1°.8$, measured West of North. The values of PD and PA measured by the individual DUs differ by less than 1σ, and are entirely consistent with each other. All measurements are above MDP_{99} [6], as certified by the fact that the 99% confidence contours in the PD–PA polar plane are closed.

The energy-dependent degree and angle of polarization in the range 2–6 keV are shown in Figure 5, while the best-fit values obtained in the different energy intervals are reported in Table 3 (along with the corresponding pulsed fraction). When the most probable value of

[6] The minimum detectable polarization at the 99% confidence level as defined in M. C. Weisskopf et al. (2010).

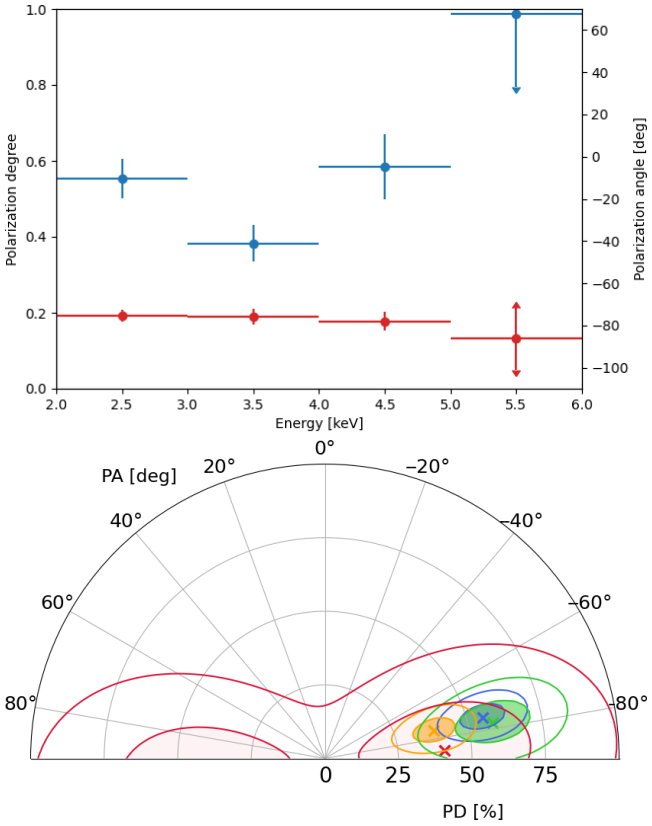

Figure 5. Top: energy-dependent polarization degree (cyan) and polarization angle (red) obtained with XSPEC (see text for details). Error bars show the 1σ confidence intervals derived with the `err` procedure. When the PD measurement falls below MDP_{99}, a downwards arrow marks the 3σ upper limit; the associated value of PA is unconstrained and is shown by a double-headed arrow. Bottom: same in the PD-PA plane for the 2–3 (blue), 3–4 (orange), 4–5 (green) and 5–6 keV (red) energy bins; symbols and contour codes are as in Figure 4. All values are reported in Table 3.

PD in a given energy interval falls below the corresponding MDP_{99} (i.e., when the corresponding 99% confidence contour remains open in the bottom panel of Figure 5), the 3σ upper limit is reported in the top panel of Figure 5, while PA is unconstrained and marked by a double arrow. Significant polarization is detected only at energies below 5 keV, which is in agreement with the discussion in section 2. In bins where the polarization measure is significant, the PD appears to vary with energy, showing a minimum between 3 and 4 keV. Taking into account also the most probable value of PD in the bin 5–6 keV, the hypothesis of a constant PD is marginally rejected at the confidence level of 94.9% ($\chi^2/\mathrm{dof} = 7.75/3$, for a fit to a constant PD). Considering, instead, only the 3 energy bins where the polarization degree is significant, the constant fit is ruled out at 97.6% confidence level ($\chi^2/\mathrm{dof} = 7.48/2$). This is supported by the confidence contours shown in Figure 5: the 68% contours of the 3–4 keV and the 2–3 keV energy bins do not intersect and the former is only tangent to the 4–5 keV one. The polarization angle, instead, is fully consistent with a constant within 1σ confidence level, with an average value of $74^\circ.4 \pm 2^\circ.1$ measured West of North.

3.5. *Phase-resolved polarimetric analysis*

In order to investigate how the polarization properties depend on the rotational phase, we folded the source photon lists into seven equally-spaced phase bins as described in §3.3, i.e. through the IXPEOBSSIM tools `xpphase` and `xpselect` and using the timing solution presented in §3.1. We then performed a simultaneous fit of the Stokes spectra within XSPEC, using a `tbabs`×(`bbodyrad`×`polconst`) model, with all spectral parameters frozen at those reported in Table 2 in the different phase bins and leaving only the `polconst` PD and PA as free parameters. The values of the best fitting parameters are reported in Table 4.

Figure 6 illustrates the phase-dependent behavior of PD and PA in the range 2–6 keV, with the corresponding pulse profile (see Figure 2) overlayed for comparison. PD is only marginally consistent with a constant ($\chi^2/\mathrm{dof} = 9.38/6$, p-value of 0.153), and the most probable values hint at an anti-correlation with the pulse profile, with the minimum (maximum) of PD occurring in the vicinity of the maximum (minimum) of the pulse profile. In contrast, the polarization angle exhibits a clear oscillation with the rotational phase, around an average value $-74^\circ.3 \pm 1^\circ.5$, consistent (within 1σ) with that derived in §3.4 (see Figure 4).

We further analyzed the data by splitting the 2–6 keV range into narrower energy intervals. After exploring different binning schemes, we found that a significant detection ($\mathrm{PD} > \mathrm{MDP}_{99}$) is obtained in all phase intervals only in the 2–3 keV and 3–6 keV bands. As shown in Figure 7, the phase-dependent polarization degree changes little in the two bands (a difference of more than 1σ appears only in the last phase bin). On the other hand, the polarization angle displays a clear oscillation in both the 2–3 and the 3–6 keV bands, consistent with the behavior in the total energy range.

We fitted the phase-dependent polarization angle with the rotating vector model (RVM, V. Radhakrishnan & D. J. Cooke 1969; M. M. Komesaroff 1970, see H. Tong et al. 2021 and R. Taverna et al. 2022 for a discussion on the RVM model applied to magnetars),

$$\tan(\mathrm{PA} - C) = \frac{\sin\xi \sin[\pm(\gamma + \gamma_0)]}{\sin\chi\cos\xi - \cos\chi\sin\xi\cos(\gamma + \gamma_0)}, \quad (1)$$

where χ and ξ are the angles of the line-of-sight (LOS) and of the magnetic axis with the spin axis, respectively,

Table 3. Energy-dependent pulsed fraction, polarization degree and angle.

Energy bin	PF [%]	PD [%]	PA [deg]	χ^2/dof
2–3 keV	$31.9^{+1.3}_{-1.3}$	$55.4^{+5.2}_{-5.2}$	$-75.4^{+2.7}_{-2.7}$	97.95/94
3–4 keV	$40.1^{+1.2}_{-1.2}$	$38.3^{+4.9}_{-4.9}$	$-75.7^{+3.7}_{-3.7}$	82.09/94
4–5 keV	$48.7^{+1.1}_{-1.1}$	$58.3^{+8.6}_{-8.6}$	$-78.0^{+4.3}_{-4.3}$	114.52/93
5–6 keV	$56.5^{+1.0}_{-1.0}$	$(40.8^{+19.3}_{-19.3})$	$(-86.2^{+176.2}_{-3.8})$	50.12/46

NOTE—PF, PD and PA values are obtained using the XSPEC procedure described in the text, with errors (at 1σ confidence level) derived from the `err` procedure in XSPEC. Negative PA values are given West of the celestial North. The most probable values of PD and PA are reported in parenthesis when PD falls below the corresponding MDP_{99}.

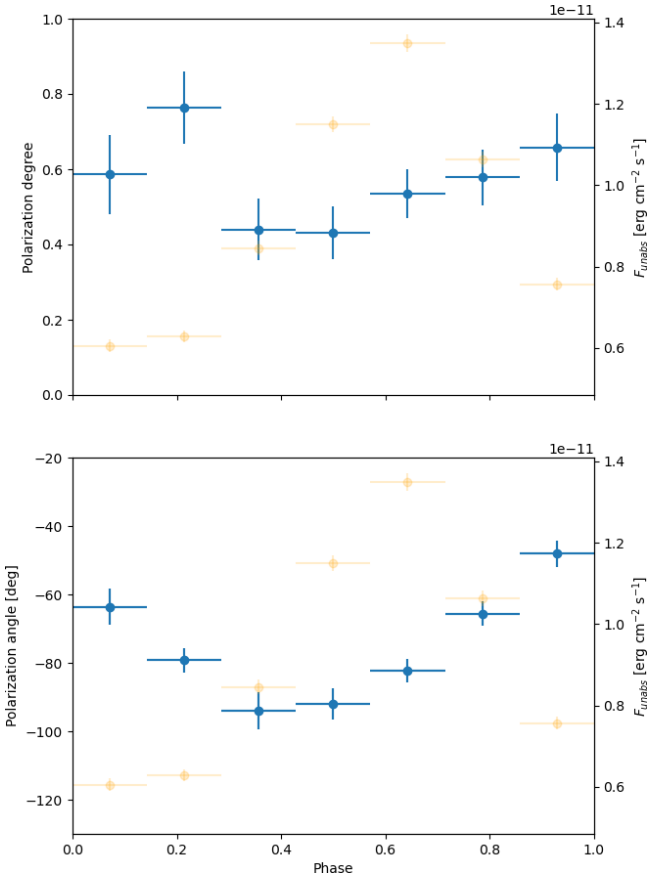

Figure 6. Phase-dependent polarization degree (top) and polarization angle (bottom), integrated over the 2–6 keV range, obtained using XSPEC (cyan, see text for details). Errors are at 1σ, as derived with the XSPEC `err` procedure. Values are reported in Table 4. In both plots, the 2–6 keV pulse profile has been superimposed for ease of comparison (light orange). A shift by $-180°$ was applied to all positive values of PA (third and fourth phase bins, see Table 4) to reproduce a smooth oscillation.

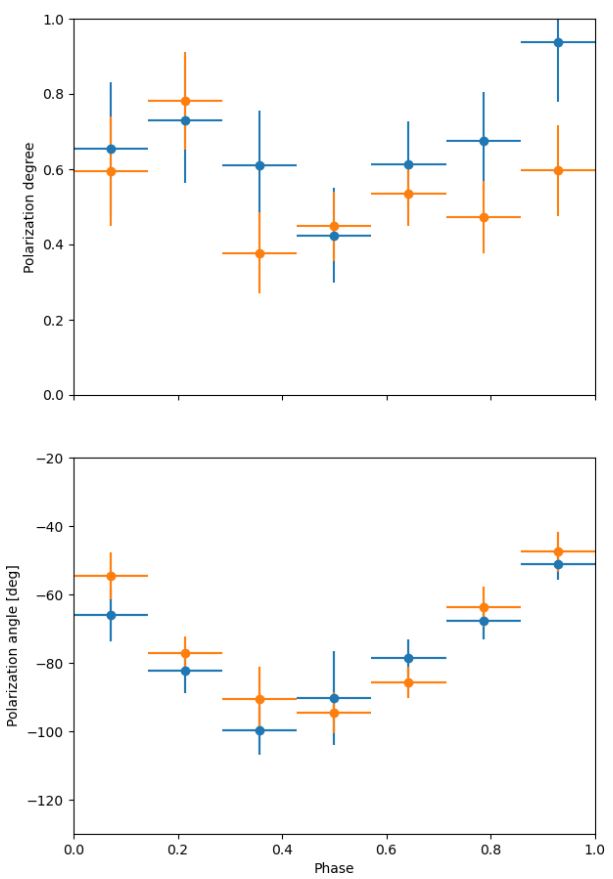

Figure 7. Phase-dependent polarization degree (top) and polarization angle (bottom), integrated over energy in the 2–3 (blue) and 3–6 keV (orange) ranges (errors are at 1σ confidence level; the error bar of PD in the last bin of the top panel is truncated at the maximum attainable value, 1). Details as in Figure 6. Values are reported in Table 4.

γ is the rotational phase, γ_0 is an arbitrary initial phase, and C is an angular offset. The plus/minus sign refers to the two possible directions of the star rotation, counter-clockwise or clockwise, and reflects the two conventions commonly adopted in the literature about the direction in which the position angle increases in the plane of the sky, clockwise/counter-clockwise if a plus/minus sign is

Table 4. Phase-resolved polarization analysis.

2–6 keV			
phase bin	PD [%]	PA [deg]	χ^2/dof
0.00–0.14	$58.6^{+10.5}_{-10.5}$	$-63.6^{+5.2}_{-5.1}$	228.53/247
0.14–0.29	$76.4^{+9.7}_{-9.7}$	$-79.2^{+3.6}_{-3.6}$	225.15/244
0.29–0.43	$44.0^{+8.2}_{-8.2}$	$86.0^{+5.4}_{-5.4}$	240.34/265
0.43–0.57	$43.1^{+7.0}_{-7.0}$	$88.0^{+4.7}_{-4.7}$	273.30/280
0.57–0.71	$53.5^{+6.4}_{-6.4}$	$-82.3^{+3.4}_{-3.4}$	258.64/294
0.71–0.86	$57.8^{+7.3}_{-7.3}$	$-65.6^{+3.6}_{-3.6}$	276.18/277
0.86–1.00	$65.8^{+9.0}_{-9.0}$	$-48.1^{+3.9}_{-3.9}$	272.99/253
2–3 keV			
phase bin	PD [%]	PA [deg]	χ^2/dof
0.00–0.14	$65.5^{+17.6}_{-17.6}$	$-66.0^{+7.7}_{-7.9}$	87.99/94
0.14–0.29	$73.1^{+16.7}_{-16.7}$	$-82.4^{+6.4}_{-6.4}$	80.74/91
0.29–0.43	$61.0^{+14.6}_{-14.6}$	$-80.2^{+6.9}_{-6.9}$	83.12/94
0.43–0.57	$42.4^{+12.6}_{-12.6}$	$89.7^{+8.6}_{-8.6}$	85.05/94
0.57–0.71	$61.2^{+11.6}_{-11.6}$	$-78.5^{+5.5}_{-5.5}$	87.49/94
0.71–0.86	$67.5^{+12.9}_{-12.9}$	$-67.7^{+5.5}_{-5.5}$	103.25/94
0.86–1.00	$93.9^{+6.1}_{-15.9}$	$-51.1^{+4.7}_{-4.7}$	88.07/94
3–6 keV			
phase bin	PD [%]	PA [deg]	χ^2/dof
0.00–0.14	$59.5^{+14.5}_{-14.5}$	$-54.7^{+7.0}_{-7.0}$	129.14/142
0.14–0.29	$78.1^{+13.1}_{-13.1}$	$-77.2^{+4.8}_{-4.8}$	139.02/142
0.29–0.43	$37.7^{+10.8}_{-10.8}$	$89.3^{+8.5}_{-8.5}$	150.40/160
0.43–0.57	$44.9^{+9.3}_{-9.3}$	$85.4^{+6.0}_{-6.0}$	181.47/175
0.57–0.71	$53.4^{+8.4}_{-8.4}$	$-85.7^{+4.5}_{-4.5}$	164.68/189
0.71–0.86	$47.3^{+9.6}_{-9.6}$	$-63.6^{+5.8}_{-5.9}$	157.96/172
0.86–1.00	$59.6^{+12.1}_{-12.1}$	$-47.5^{+5.9}_{-5.9}$	172.56/148

NOTE—Results are obtained using the XSPEC procedure described in the text. Errors are at 1σ confidence level, derived from the `err` procedure in XSPEC. PA values are given East of the celestial North.

placed in front of the fraction in equation (1), in lieu of the plus/minus sign inside the sine function (J. E. Everett & J. M. Weisberg 2001). For the sake of conciseness, we will refer to the two possible choices for the RVM models as the "plus" (χ_+, ξ_+) and "minus" (χ_-, ξ_-) solutions. It should be noted that, due to the π-periodicity of the arctan function, the configurations $(2\pi - \chi_\pm, 2\pi - \xi_\pm)$, i.e. $(-\chi_\pm, -\xi_\pm)$, describe equivalent geometries. In order to improve the statistics, we fitted simultaneously the data integrated in the 2–3 and in the 3–6 keV band, treating the two datasets as mutually independent. This is justified on the assumption that the recorded events are Poissonian distributed and the events collected in separate energy channels are physically distinct. Leaving all four parameters in equation (1) free to vary, the best simultaneous fits yield $\chi_+ = 106°.6 \pm 30°.9$ and $\xi_+ = 157°.7 \pm 4°.0$ for the plus solution and $\chi_- = -73°.4$, $\xi_- = -22°.3$ for the minus one (see Table 5 and Figure 8 for more details). Both pairs of angles provide the same, good fit to the observed PA and, as expected, it is $\xi_- = \xi_+ - \pi$, $\chi_- = \chi_+ - \pi$, which exactly mirrors the two spin orientations. We also verified that the fits of PA integrated throughout the 2–6 keV band yield consistent results within the errors.

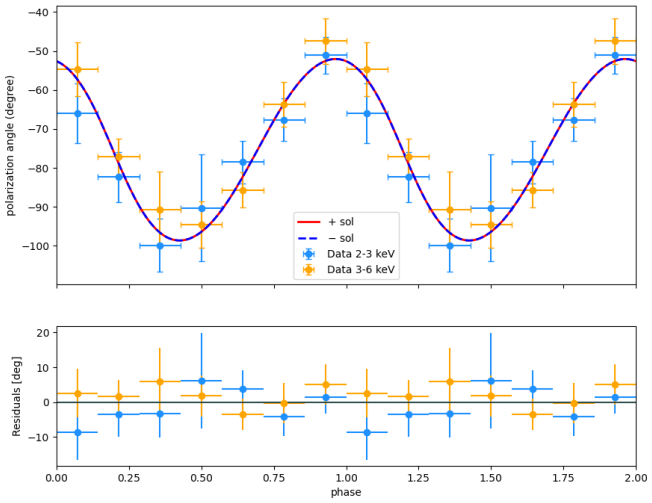

Figure 8. *IXPE* 2–3 keV (cyan) and 3–6 keV (orange) polarization angle simultaneously fitted by a rotating vector model (see Table 5); two rotational cycles are shown for ease of visualization. The red solid (blue dotted) line shows the best fitting plus (minus) solution; residuals are shown in the bottom panel.

We corroborated our RVM results with a Bayesian analysis, starting from flat priors in the range $[0, 2\pi]$ for the plus solution, $[-\pi, \pi]$ for the minus solution, $[-2\pi, 2\pi]$ for C and γ_0. The posteriors for the two models are shown in Figure 9; the probability density distributions are clearly the same, much as the best fitting models in Figure 8, with the only difference of a shift by $-\pi$ in the χ, ξ angles. The best estimates for the parameters derived with both techniques are in close agreement, well within 1σ uncertainties.

Although the RVM fitting provides a well constrained value of the angle ξ between the rotation and the dipole axis, the angle χ between the rotation axis and the LOS is more loosely determined, with an uncertainty of $\sim 30°$. Despite these limitations, both solutions point to an inclined rotator seen away from the spin axis. This is at variance with the geometry reported by R. E. Stewart et al. (2025b), $\chi = 5°.2^{+3.2}_{-2.6}$ and $\xi = 2°.4^{+1.4}_{-1.2}$, based on simultaneous Parkes/Murriyang radio data. Our solution for the inclination of the dipole axis, $\xi_+ \sim 158°$, is close to the best estimate, $\xi = 160°$, reported by F. Camilo et al. (2008), using two distinct 2007 Parkes radio observations covering roughly half of the rotational period. However, the value they derived for the inclination of the spin axis, $\chi = 174°$, is different. We also note that a geometry with ($\chi = 174°$, $\xi = 160°$) is inconsistent with the oscillating behavior of PA observed in the radio, since the RVM model with $\chi > \xi$ (χ, $\xi > 90°$) swings from $-90°$ to $90°$. A reanalysis of the same 2007 Parkes data by R. E. Stewart et al. (2025b) sug-

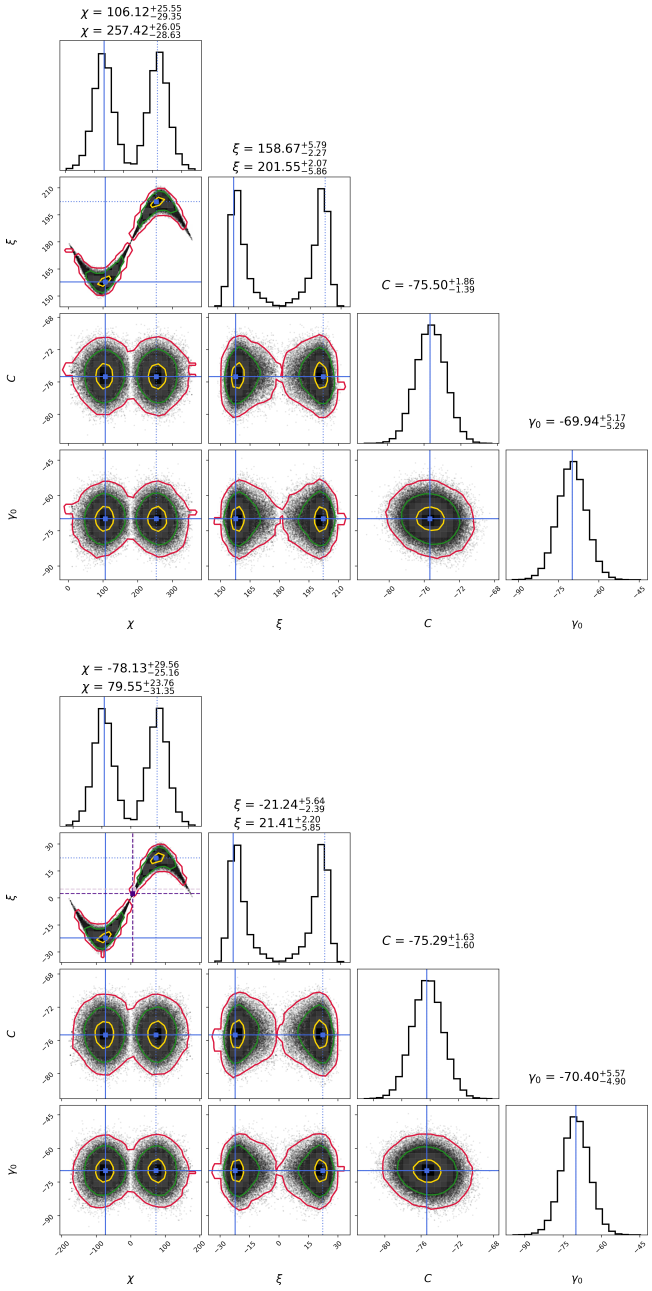

Figure 9. Marginalized posterior distributions for the RVM plus (top) and minus (bottom) solutions. The best-fit values $(\chi_\pm, \xi_\pm)$, obtained through χ^2 minimization, as well as the mirrored solutions $(2\pi - \chi_\pm, 2\pi - \xi_\pm)$ are marked by solid and dotted blue lines, respectively. The 1, 2, and 3σ confidence contours are shown in yellow, green, and red, respectively. The maximum a posteriori estimates, along with their associated 1σ uncertainties, are reported above each 1D histogram. The best-fit values from the radio analysis by R. E. Stewart et al. (2025b), $\chi = 5°.2, \xi = 2°.4$ (dashed violet lines) and $\chi = 8°.4, \xi = 4°.9$ (dashed pink lines), are also shown for comparison.

gested a low-obliquity solution, with $\chi = 8^\circ.4^{+5.8}_{-4.2}$ and $\xi = 4^\circ.9^{+3.4}_{-2.4}$.

4. DISCUSSION

Despite the shorter exposure, compared to those of the other magnetars targeted by *IXPE* (only 1E 1841−045 was observed for a comparable time; M. Rigoselli et al. 2025; R. E. Stewart et al. 2025a), we were able to perform timing, spectral, and polarization analyses of 1E 1547.0−5408, obtaining significant measurements in the 2–6 keV energy band; at higher energies, the background dominates the signal, preventing any meaningful conclusion.

The phase-averaged spectrum turns out to be well described by a single blackbody component with temperature ~ 0.7 keV. Folding the data in seven, equally-spaced phase intervals, the same spectral model provides a good representation in every phase bin. However, a variation of the temperature with the rotational phase is clearly present, which closely follows the flux modulation, while the emission radius is consistent with being a constant (see Figures 2 and 3). The single-peaked, quasi-sinusoidal pulse shape, the relatively large pulsed fraction, which increases with energy (see Table 3), and the small blackbody radius (~ 1.2 km) point to a single, fairly small hot-spot. The change of $T_{\rm BB}$ along the rotation suggests a complex emission pattern, with radiation coming from a region on the star surface characterized by a non-uniform temperature distribution, with colder and hotter zones entering in view at different phases.

The large phase- and energy-integrated polarization degree measured by *IXPE* ($\approx 50\%$) places 1E 1547.0−5408 alongside the mostly polarized magnetars, 1RXS J1708 (S. Zane et al. 2023) and 1E 1841−045 (M. Rigoselli et al. 2025), the properties of which were interpreted in terms of an atmospheric layer covering the emitting region. The same explanation possibly holds also for 1E 1547.0−5408. In fact, the energy-dependent PD (see Figure 5) reaches values as high as $\approx 60\%$, which is incompatible with thermal emission from a bare condensed surface around 2–3 keV and magnetospheric reprocessing via RCS at higher energies (R. Taverna et al. 2020, besides, no evidence for a power-law tail was found in the *IXPE* data).

Although an atmosphere can explain the spectral properties and the large observed PD in 1E 1547.0−5408, the possible presence of a local minimum in the degree of polarization between 3 and 4 keV, if confirmed, poses a challenge, as there is no evidence of a second spectral component or prominent spectral features that can explain such behavior [7]. R. E. Stewart et al. (2025b) invoke mode conversion at the vacuum resonance (VR; see G. G. Pavlov & Y. A. Shibanov 1979; A. D. Kaminker et al. 1982; W. C. G. Ho & D. Lai 2003) to explain the decrease in PD, which they estimate to vanish at about 6 keV, with a 90° swing of the polarization angle at the same energy. However, our analysis shows no evidence of either a monotonic decrease with energy or a vanishing polarization at high energies. Indeed, a linear fit to the energy-dependent PD forcing the slope to be negative yields a $\chi^2/{\rm dof} = 7.429/2$, and still predicts a PD $\approx 40\%$ at 6 keV, while PA is consistent with being a constant.

Still, the occurrence of mode switching at the VR does not necessarily imply a change in the dominant mode (i.e. a 90° swing in PA). For magnetic fields as high as $\approx 2 \times 10^{14}$ G (the spin-down field of 1E 1547.0−5408, see §3.1), mode switching can be partial, meaning that not all O-mode photons become X-mode ones (and conversely) at the VR, with the probability of switching between modes depending on the energy of the photon, magnetic field, and density gradient in the atmosphere (W. C. G. Ho & D. Lai 2003). This results in a local minimum in PD, while the polarization angle remains constant with energy (R. M. E. Kelly et al. 2024, 2025, and references therein). To test whether (partial) mode conversion at the vacuum resonance can produce a behavior of PD like that suggested by *IXPE* between 3 and 4 keV, we performed some simulations following the method detailed in R. M. E. Kelly et al. (2024). Figure 10 shows the energy-dependent behavior of the polarization degree in the case of emission from a single atmospheric patch, assuming a field of strength $B = 2 \times 10^{14}$ G, inclined by $\sim 10^\circ$ wrt the surface normal and a probability threshold of $P_{\rm th} = 0.9$ [8] Although a more detailed model is required before any definitive conclusion can be drawn, the results reported in Figure 10 suggest that partial mode conversion at the VR can produce dips in PD at the energies observed by *IXPE* in 1E 1547.0−5408.

[7] Especially for small emitting spots, propagation across the Quasi-Tangential (QT) region, where the photon propagation direction is nearly parallel to the magnetic field lines, can reduce the observed PD. However, the depolarization occurs at energies well below the *IXPE* band for magnetic fields $\gtrsim 10^{14}$ G (C. Wang & D. Lai 2009).

[8] The magnetic field used in the simulation of Figure 10 is somewhat smaller than the polar value inferred in 1E 1547.0−5408, because convergence issues with our atmospheric code prevented us from reaching higher values of B. We successfully produced a run with an aligned field of $B = 4 \times 10^{14}$ G on a coarser energy grid which, albeit noisier, is consistent with the results shown in Figure 10.

Table 5. RVM fit of the polarization angle.

	χ (deg)	ξ (deg)	C (deg)	γ_0 (deg)	χ^2/dof
plus solution	106.60 ± 30.85	157.73 ± 4.04	-75.35 ± 1.62	-69.93 ± 5.15	5.227/10
minus solution	-73.40 ± 30.85	-22.27 ± 4.04	-75.35 ± 1.62	-69.93 ± 5.15	5.227/10

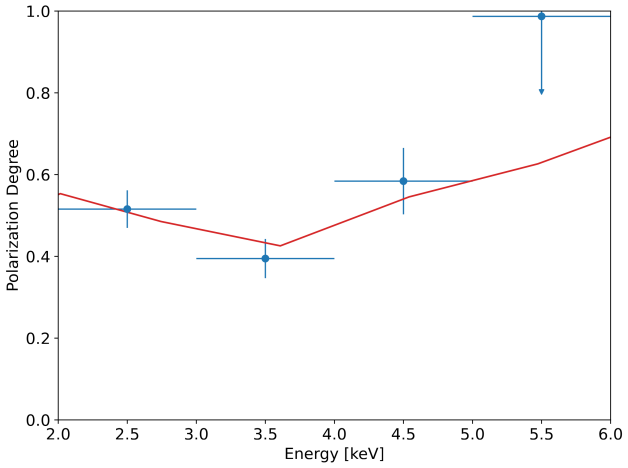

Figure 10. Energy-dependent polarization degree (red) at the surface of an atmospheric patch including partial mode conversion at the VR. Here, the inclination of the magnetic field to the surface normal is $\sim 10^\circ$ and the field strength 2×10^{14} G. The observed polarization degree is also shown (cyan) to facilitate visual comparison.

The phase variation of PD is statistically consistent with a constant within 1σ uncertainties. However, the most probable values hint to an anti-correlation of PD with the pulse profile in the total band (2–6 keV), and also in the 2–3 and 3–6 keV energy intervals (see the top panels of Figures 6 and 7). On the other hand, the polarization angle traces a clean sinusoidal modulation with the rotational phase, which can be well fitted with a rotating vector model (see Figure 8). This pattern is common to other magnetars observed by *IXPE* and has been interpreted as a signature of vacuum birefringence in the external region close to the star (R. Taverna et al. 2022; S. Zane et al. 2023; J. Heyl et al. 2024). While PD bears the imprint of the (complex) thermal and magnetic maps on the star surface, much as the pulse profile, PA is determined at larger distances where the topology of the field is largely dipolar. This is a consequence of vacuum birefringence, which forces the polarization vectors to follow the magnetic field direction up to the polarization-limiting radius ($r_{\rm pl} \approx 100\,R_{\rm NS}$ for magnetars; J. S. Heyl et al. 2003; R. Taverna et al. 2015).

According to R. E. Stewart et al. (2025b), who fitted the polarization angle measured in the radio band with the Parkes/Murriyang telescope, the star is an almost aligned rotator, seen nearly along the magnetic axis. In this case, for photons coming from regions very close to the pole, the polarization vectors at emission would co-rotate with the star, following the magnetic field near the pole. As a consequence, if vacuum birefringence is neglected, the phase-averaged polarization degree observed at infinity should be significantly lower than what is expected when a proper account for QED effects is made, even assuming that emitted photons are polarized mostly in one mode. This is one of the points that led R. E. Stewart et al. (2025b) to claim that the high phase-averaged and phase-resolved polarization degree detected by *IXPE* in 1E 1547.0−5408 is a compelling test of vacuum birefringence.

Our RVM fit of PA measured by *IXPE* produces a different geometry, with a net inclination between the magnetic and rotation axes of $\sim 20^\circ$ and the LOS tilted by $\sim 75^\circ$ wrt the rotation axis. The nearly aligned geometries proposed by R. E. Stewart et al. (2025b) are, according to our posteriors, excluded with significance $\gtrsim 90\%$.

In the geometry we found, the difference in the degree of polarization obtained with or without accounting for vacuum birefringence is expected to be negligible because of the limited extent of the emission region and of the strong magnetic field of the source. In such cases, in fact, the change in the magnetic field direction across the emitting area is quite small, mimicking the conditions that would generally occur at a large distance from the source ($r_{\rm pl} \approx 100 R_{\rm NS}$, C. Wang & D. Lai 2009).

To provide a quantitative estimate, we performed a simulation using the ray-tracing code discussed in R. Taverna et al. (2015). General relativistic corrections, both in the photon trajectories and in the magnetic field, are accounted for. We assumed a neutron star mass and radius of $M = 1.4\,M_\odot$ and $R = 12$ km, respectively, and a (polar) value of the dipole field $B \sim 5 \times 10^{14}$ G. The emission comes from a circular spot centered on the magnetic pole with semi-aperture $\theta \approx 6^\circ$, corresponding to $R_{\rm BB} \approx 1.2$ km (as evaluated by a distant observer, see

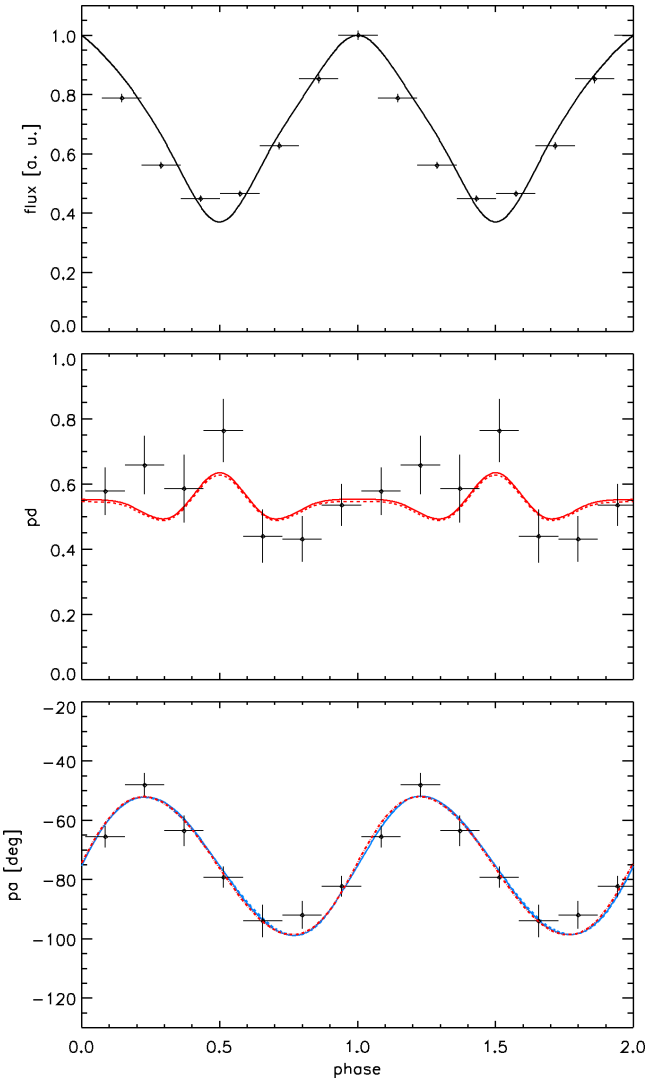

Figure 11. Pulse profile (normalized to the maximum, top), phase-dependent PD (middle) and PA (bottom) as obtained from the ray-tracing code discussed in R. Taverna et al. (2015), using χ_- and ξ_- (red dash-dotted line in the bottom panel). The emitting region is a circular spot at the magnetic pole (see text for details). Solid and dashed lines show the results obtained with and without including vacuum birefringence effects, respectively. *IXPE* data are also shown (black points with error bars). Both flux and PD/PA points have been phase-shifted back by ≈ 0.65 cycles wrt Figures 2, 6 and 7 to facilitate visual comparison.

Table 1). The spot is divided into a hot ($kT_{\rm h} = 0.87$ keV, $\theta_{\rm h} \approx 3°$) cap with a large intrinsic polarization (80%), surrounded by a warm ($kT_{\rm w} = 0.76$ keV) annulus, extending from 3° to 6°, with a lower polarization (30%); the rest of the surface is cold, at $kT_{\rm c} = 0.15$ keV. Both regions emit isotropic blackbody radiation and the (constant) polarization degrees were chosen in such a way to recover the observed PD in the *IXPE* band. All previous quantities are measured by a stationary observer at the star surface, unless explicitly stated otherwise.

The results, shown in Figure 11 for our geometry, are qualitatively in agreement with the *IXPE* measurements in the 2–6 keV band, and successfully reproduce the single-peaked pulse profile, a nearly constant phase-dependent polarization degree (weakly anti-correlated with the light curve), and a clear sinusoidal oscillation of the polarization angle. Actually, emission from a more realistic magnetized atmosphere model is not expected to be isotropic. In order to test if and to which extent magnetic beaming can influence the results presented in Figure 11, we computed some models replacing the Planck function, B_ν, with $B_\nu f(\mu)$, where $\mu = \cos\theta_{\rm Bk}$ is the cosine of the angle between the local magnetic field and the ray. The beaming factor $f(\mu)$ was taken to qualitatively reproduce the angular pattern of the intensity emerging from a strongly magnetized atmosphere (e.g. F. Özel 2001). However, only small deviations in the pulse profiles were found: fractional differences in the pulsed fraction are typically $\lesssim 10\%$) while both PD and PA are pretty much unchanged. At any rate, and as for the model shown in Figure 10, we stress that this simple model is not intended to faithfully match all the observed features, but rather to demonstrate that the derived viewing geometry and emission configuration produce results consistent with the observations. As expected, the polarization degree calculated with or without considering vacuum birefringence (solid and dashed lines in the central panel) is nearly indistinguishable, so no compelling argument about the presence of vacuum birefringence can be made.

In this respect, it is worth drawing some comparisons between our analysis and that of the magnetar 1RXS J1708 presented in S. Zane et al. (2023). Here we have shown that a simple emission model, which relies on the source geometry inferred from the RVM fit of the *IXPE* polarization angle, can broadly reproduce the main X-ray properties of the source. In the case of 1RXS J1708, a somewhat reverse approach was followed. First, possible emission geometries capable of explaining the (energy-dependent) spectro-polarimetric data were explored, and then these were contrasted with the phase variation of PA and with the RVM best fit. The agreement they found is only qualitative, not surprisingly given that no real fit of PA with their models was attempted.

The relatively large half-opening angle of the radio beam required by our X-ray-favored geometry to match the observed duty cycle ($\rho \sim 22°$) does not necessarily invalidate the model. Although the empirical relation $\rho \sim 5°/\sqrt{P}$ predicts a much narrower beam ($\sim 3.4°$ for

a period 2.1 s), this scaling is derived primarily from ordinary rotation-powered pulsars. 1E 1547.0−5408 is a high-energy magnetar with a rotational loss rate ($\dot{E} \sim 9 \times 10^{34}$ erg/s) and magnetic field strength far exceeding the population used to establish such relations. Given the significant scatter in beam widths observed even among ordinary pulsars (see e.g. S. Johnston & A. Karastergiou 2019), and the unique magnetospheric physics of magnetars, an opening angle $\rho \sim 22°$ cannot be ruled out.

5. CONCLUSIONS

In this work, we presented an analysis of the 500 ks *IXPE* observation of the AXP 1E 1547.0−5408. We found that the source X-ray emission is essentially thermal, with only one blackbody component contributing at each phase of the star rotation, and comes from a fairly limited region on the star surface ($R_{\rm BB} \approx 1.2$ km) with non-uniform properties, as suggested by the modulation of the temperature with phase.

Both the relatively high phase-averaged and phase-resolved polarization degrees are consistent with emission from a magnetized atmospheric layer covering (part of) the star surface. The constancy of the polarization angle with energy implies that radiation is polarized in the same mode throughout the *IXPE* band, as predicted for an ultra-magnetized atmosphere, the emission of which is expected to be X-mode dominated (R. M. E. Kelly et al. 2024). The only potential evidence of QED effects in the atmospheric medium (vacuum+plasma) comes from the dip in the degree of polarization that is possibly present around 3–4 keV, which may indeed be a signature of partial mode conversion at the vacuum resonance.

On the other hand, the rotating vector model provides a very good interpretation of the modulation in phase of the polarization angle measured by *IXPE* and this hints at the presence of vacuum birefringence in the star magnetosphere (R. Taverna et al. 2022). In the geometry we inferred from the RVM fit, 1E 1547.0−5408 is an inclined rotator seen nearly perpendicular to the spin axis and this is consistent with the observed pulse profile, assuming isotropic thermal emission from a polar hot spot on the star surface. The geometry derived by R. E. Stewart et al. (2025b) from radio data points to an almost aligned rotator seen close to the pole, which is unlikely on the basis of *IXPE* data alone. Still, given that it falls at the boundary of our 3σ contour (see Figure 9), it cannot be excluded, potentially removing the tension between the measures in the two bands. On the other hand, since the rotating vector model constrains the source geometry independently of the assumed emission model, the magnetic field topology in the regions responsible for the radio and the X-ray emission may be different. Further multi-wavelength observations of 1E 1547.0−5408 are needed to clarify this issue.

The actual source geometry has an impact on the conclusions one can draw about the presence of QED effects. In the case of an inclined geometry, as the one derived here, the polarization degree of radiation emitted from a small spot is maintained up to the observer for magnetar-like fields, and no claim about the presence of vacuum birefringence can be made, no matter how large the polarization degree is. In this respect, 1E 1547.0−5408 is not different from other persistent magnetars observed in polarized X-rays (e.g., 1RXS J1708 and 1E 1841−045), confirming that such sources are not ideal targets for (indirect) tests of QED, unless the emission comes from a reasonably extended portion of the surface.

A significant step forward is expected from observations of transient magnetars in outburst, during which emission is indeed expected to emerge from wide hot spots. Another promising class of sources is that of X-ray Dim Isolated Neutron Stars (XDINSs), which are also strongly magnetized (albeit with fields typically an order of magnitude lower than those of magnetars, see R. Turolla 2009), the prototypical and brightest member of which, RX J1856.5−3754, exhibits a very low X-ray pulsed fraction (N. Sartore et al. 2012), making them key targets for testing vacuum birefringence with future instruments capable of probing polarization at sub-keV energies (see e.g. R. M. E. Kelly et al. 2025, for predictions in the soft X-rays and R. P. Mignani et al. 2017 for a potential QED detection in the optical). Next-generation X-ray polarimeters, like *eXTP* (the Enhanced X-ray Timing and Polarimetry mission, S.-N. Zhang et al. 2025), *EXPO* (the Enhanced X-ray Polarimetry Observatory, recently proposed for the ESA medium-size mission call), with their superior sensitivity and fast-repointing capabilities in the medium-to-high energy X-ray band, and GOSoX (the Globe Orbiting Soft X-ray polarimeter concept, H. L. Marshall et al. 2021), which will observe in the soft-X band, will hopefully provide the definitive answer on the long-sought-after test of vacuum birefringence, finally bridging the gap between fundamental physics and astrophysical observations of neutron stars.

ACKNOWLEDGMENTS

We gratefully acknowledge an anonymous referee for their constructive criticism and helpful remarks. This research was supported by the International Space Sci-

ence Institute (ISSI) in Bern, through the International Team project 25-657 “Polarimetric Insights into Extreme Magnetism”. The work of R. Ta., R. Tu. and L. M. is partially funded by the PRIN 2022 - project 2022LWPEXW - “An X-ray view of compact objects in polarized light”, European Union funding - Next Generation EU, Mission 4 Component 1, CUP C53D23001180006. R.M.E. K. is supported by The Science and Technology Facilities Council (STFC) via a PhD studentship (grant number ST/W507891/1). GL. I. and S. M. acknowledge financial support from INAF through the Bando Ricerca Fondamentale INAF 2024, Large Grant “TULiP” and GO Grant “Toward Neutron Stars Unification”, respectively. A. B. acknowledges support through the European Space Agency (ESA) research fellowship program.

REFERENCES

Arnaud, K. A. 1996, in Astronomical Society of the Pacific Conference Series, Vol. 101, Astronomical Data Analysis Software and Systems V, ed. G. H. Jacoby & J. Barnes, 17

Bachetti, M. 2018, HENDRICS: High ENergy Data Reduction Interface from the Command Shell,, Astrophysics Source Code Library, record ascl:1805.019 http://ascl.net/1805.019

Bachetti, M., Harrison, F. A., Cook, R., et al. 2015, ApJ, 800, 109, doi: 10.1088/0004-637X/800/2/109

Baldini, L., Bucciantini, N., Lalla, N. D., et al. 2022, ixpeobssim: Imaging X-ray Polarimetry Explorer simulator and analyzer,, Astrophysics Source Code Library, record ascl:2210.020 http://ascl.net/2210.020

Bernardini, F., Israel, G. L., Stella, L., et al. 2011, A&A, 529, A19, doi: 10.1051/0004-6361/201016197

Camilo, F., Reynolds, J., Johnston, S., Halpern, J. P., & Ransom, S. M. 2008, ApJ, 679, 681, doi: 10.1086/587054

Chen, C.-T., & IXPE Science Operation Center. 2025, in American Astronomical Society Meeting Abstracts, Vol. 245, American Astronomical Society Meeting Abstracts #245, 260.01

Coti Zelati, F., Rea, N., Pons, J. A., Campana, S., & Esposito, P. 2018, MNRAS, 474, 961, doi: 10.1093/mnras/stx2679

Coti Zelati, F., Borghese, A., Rea, N., et al. 2020, A&A, 633, A31, doi: 10.1051/0004-6361/201936317

De Grandis, D., Turolla, R., Taverna, R., et al. 2022, ApJ, 936, 99, doi: 10.3847/1538-4357/ac8797

Di Marco, A., Soffitta, P., Costa, E., et al. 2023, AJ, 165, 143, doi: 10.3847/1538-3881/acba0f

Duncan, R. C., & Thompson, C. 1992, ApJL, 392, L9, doi: 10.1086/186413

Everett, J. E., & Weisberg, J. M. 2001, ApJ, 553, 341, doi: 10.1086/320652

Fernández, R., & Davis, S. W. 2011, ApJ, 730, 131, doi: 10.1088/0004-637X/730/2/131

Fernández, R., & Thompson, C. 2007, ApJ, 660, 615, doi: 10.1086/511810

Gnedin, Y. N., Pavlov, G. G., & Shibanov, Y. A. 1978a, Soviet Journal of Experimental and Theoretical Physics Letters, 27, 305

Gnedin, Y. N., Pavlov, G. G., & Shibanov, Y. A. 1978b, Soviet Astronomy Letters, 4, 117

Harding, A. K., & Lai, D. 2006, Reports on Progress in Physics, 69, 2631, doi: 10.1088/0034-4885/69/9/R03

Heyl, J., Taverna, R., Turolla, R., et al. 2024, MNRAS, 527, 12219, doi: 10.1093/mnras/stad3680

Heyl, J. S., & Hernquist, L. 1997, Journal of Physics A Mathematical General, 30, 6485, doi: 10.1088/0305-4470/30/18/022

Heyl, J. S., Shaviv, N. J., & Lloyd, D. 2003, MNRAS, 342, 134, doi: 10.1046/j.1365-8711.2003.06521.x

Ho, W. C. G., & Lai, D. 2003, MNRAS, 338, 233, doi: 10.1046/j.1365-8711.2003.06047.x

Johnston, S., & Karastergiou, A. 2019, MNRAS, 485, 640, doi: 10.1093/mnras/stz400

Kaminker, A. D., Pavlov, G. G., & Shibanov, I. A. 1982, Ap&SS, 86, 249, doi: 10.1007/BF00683336

Kaspi, V. M., & Beloborodov, A. M. 2017, ARA&A, 55, 261, doi: 10.1146/annurev-astro-081915-023329

Kelly, R. M. E., Marshall, H. L., Zane, S., et al. 2025, ApJ, 987, 113, doi: 10.3847/1538-4357/adde58

Kelly, R. M. E., Zane, S., Turolla, R., & Taverna, R. 2024, MNRAS, 528, 3927, doi: 10.1093/mnras/stae159

Komesaroff, M. M. 1970, Nature, 225, 612, doi: 10.1038/225612a0

Lai, D. 2023, Proceedings of the National Academy of Science, 120, e2216534120, doi: 10.1073/pnas.2216534120

Lower, M. E., Younes, G., Scholz, P., et al. 2023, ApJ, 945, 153, doi: 10.3847/1538-4357/acbc7c

Luo, J., Ransom, S., Demorest, P., et al. 2021, ApJ, 911, 45, doi: 10.3847/1538-4357/abe62f

Manchester, R. N., Hobbs, G. B., Teoh, A., & Hobbs, M. 2005, AJ, 129, 1993, doi: 10.1086/428488

Marshall, H. L., Heine, S. N. T., Garner, A., et al. 2021, in Society of Photo-Optical Instrumentation Engineers (SPIE) Conference Series, Vol. 11444, Society of Photo-Optical Instrumentation Engineers (SPIE) Conference Series, ed. J.-W. A. den Herder, S. Nikzad, & K. Nakazawa, 114442Y, doi: 10.1117/12.2562811

Mignani, R. P., Testa, V., González Caniulef, D., et al. 2017, MNRAS, 465, 492, doi: 10.1093/mnras/stw2798

Nobili, L., Turolla, R., & Zane, S. 2008, MNRAS, 386, 1527, doi: 10.1111/j.1365-2966.2008.13125.x

Özel, F. 2001, ApJ, 563, 276, doi: 10.1086/323851

Pavlov, G. G., & Shibanov, Y. A. 1979, Soviet Journal of Experimental and Theoretical Physics, 49, 741

Piconcelli, E., Jimenez-Bailón, E., Guainazzi, M., et al. 2004, MNRAS, 351, 161, doi: 10.1111/j.1365-2966.2004.07764.x

Radhakrishnan, V., & Cooke, D. J. 1969, Astrophys. Lett., 3, 225

Rigoselli, M., Taverna, R., Mereghetti, S., et al. 2025, ApJL, 985, L34, doi: 10.3847/2041-8213/adbffb

Sartore, N., Tiengo, A., Mereghetti, S., et al. 2012, A&A, 541, A66, doi: 10.1051/0004-6361/201118489

Stewart, R. E., Younes, G. A., Harding, A. K., et al. 2025a, ApJL, 985, L35, doi: 10.3847/2041-8213/adbffa

Stewart, R. E., Dinh Thi, H., Younes, G., et al. 2025b, arXiv e-prints, arXiv:2509.19446, doi: 10.48550/arXiv.2509.19446

Strohmayer, T. E. 2017, ApJ, 838, 72, doi: 10.3847/1538-4357/aa643d

Taverna, R., Muleri, F., Turolla, R., et al. 2014, MNRAS, 438, 1686, doi: 10.1093/mnras/stt2310

Taverna, R., & Turolla, R. 2024, Galaxies, 12, 6, doi: 10.3390/galaxies12010006

Taverna, R., Turolla, R., Gonzalez Caniulef, D., et al. 2015, MNRAS, 454, 3254, doi: 10.1093/mnras/stv2168

Taverna, R., Turolla, R., Suleimanov, V., Potekhin, A. Y., & Zane, S. 2020, MNRAS, 492, 5057, doi: 10.1093/mnras/staa204

Taverna, R., Turolla, R., Muleri, F., et al. 2022, Science, 378, 646, doi: 10.1126/science.add0080

Thompson, C., & Duncan, R. C. 1993, ApJ, 408, 194, doi: 10.1086/172580

Thompson, C., Lyutikov, M., & Kulkarni, S. R. 2002, ApJ, 574, 332, doi: 10.1086/340586

Tiengo, A., Vianello, G., Esposito, P., et al. 2010, ApJ, 710, 227, doi: 10.1088/0004-637X/710/1/227

Tong, H., Wang, P. F., Wang, H. G., & Yan, Z. 2021, MNRAS, 502, 1549, doi: 10.1093/mnras/stab108

Turolla, R. 2009, in Astrophysics and Space Science Library, Vol. 357, Astrophysics and Space Science Library, ed. W. Becker, 141, doi: 10.1007/978-3-540-76965-1_7

Turolla, R., Zane, S., & Watts, A. L. 2015, Reports on Progress in Physics, 78, 116901, doi: 10.1088/0034-4885/78/11/116901

Turolla, R., Taverna, R., Israel, G. L., et al. 2023, ApJ, 954, 88, doi: 10.3847/1538-4357/aced05

Verner, D. A., Ferland, G. J., Korista, K. T., & Yakovlev, D. G. 1996, ApJ, 465, 487, doi: 10.1086/177435

Wang, C., & Lai, D. 2009, MNRAS, 398, 515, doi: 10.1111/j.1365-2966.2009.14895.x

Weisskopf, M. C., Guainazzi, M., Jahoda, K., et al. 2010, ApJ, 713, 912, doi: 10.1088/0004-637X/713/2/912

Weisskopf, M. C., Soffitta, P., Baldini, L., et al. 2022, Journal of Astronomical Telescopes, Instruments, and Systems, 8, 1 , doi: 10.1117/1.JATIS.8.2.026002

Wilms, J., Allen, A., & McCray, R. 2000, ApJ, 542, 914, doi: 10.1086/317016

Zane, S., Taverna, R., González-Caniulef, D., et al. 2023, ApJL, 944, L27, doi: 10.3847/2041-8213/acb703

Zhang, S.-N., Santangelo, A., Xu, Y., et al. 2025, Science China Physics, Mechanics, and Astronomy, 68, 119502, doi: 10.1007/s11433-025-2786-6